RESEARCH ARTICLE | SEPTEMBER 27 2018

Influence of electron backflow on discharge asymmetry in atmospheric helium dielectric barrier discharges

Yuhui Zhang; Dong Dai ; Wenjun Ning ; Licheng Li

AIP Advances 8, 095327 (2018)
https://doi.org/10.1063/1.5016401

Influence of electron backflow on discharge asymmetry in atmospheric helium dielectric barrier discharges

Yuhui Zhang, Dong Dai, Wenjun Ning,[a] and Licheng Li
School of Electric Power, South China University of Technology, Guangzhou 510641, China

(Received 18 November 2017; accepted 18 September 2018;
published online 27 September 2018)

In this paper, the transition mechanisms between symmetric and asymmetric discharges in atmospheric helium dielectric barrier discharges (DBDs) are investigated via a one-dimensional fluid model. By gradually increasing the gap width, a complete evolution trajectory of the discharge states (i.e. from symmetric single period discharge (SP1) to asymmetric single-period (AP1) discharge, finally returns back to SP1 discharge) is observed. Unlike the previous reports which emphasize the dominant role of residual positive column, this work demonstrates that the transitions between SP1 and AP1 discharges could also be induced by the electron backflow effect. It is the residual electron backflow region that provides extra seed electrons to the subsequent discharge, restraining the development of electric field in the breakdown process, thus weakening the next discharge pulse. Upon the impairment of one discharge pulse, due to the reduction of charge generation and the impairment of electron backflow effect in the relevant discharge phase, its subsequent discharge would be strengthened. Those mechanisms function in different current pulses at different gap widths, inducing the mode transition. In addition, our simulation result reveals that the "residual positive column" referred in previous publications is essentially a special form of the "electron backflow region", which is typically more remarkable in large gap widths. As a consequence, the dynamics of electron backflow provides more insights regarding the transition of nonlinear states in DBDs with controlling parameters varying. https://doi.org/10.1063/1.5016401

I. INTRODUCTION

Recent years have witnessed tremendous development of atmospheric pressure dielectric barrier discharge (DBD) in theoretical studies[1–7] as well as applications.[8–13] As an effective tool to produce homogeneous plasma at atmospheric pressure, DBD has presented its immense potentials for numerous industrial applications, thus being the subject of intense research over the world. Typically, DBD manifests itself as a symmetric single-period (SP1) discharge under symmetric discharge structure, in which the discharge current repeats exactly at one period of applied voltage, and the shape and amplitude of positive and negative current pulses are identical.[14–16] However, as a nonlinear dynamic system, there are many kinds of nonlinear phenomena emerging in DBDs or DBD derived plasmas under certain conditions, including period doubling bifurcation, quasi-period and chaos,[17–20] while the subtle mechanisms of those phenomena are far from being understood.

In fact, before the discharge evolves into above-mentioned nonlinear dynamic states, it would always bifurcate into an asymmetric single-period (AP1) discharge at the first step.[14–16,21–24] In an AP1 discharge, the positive and negative current pulses differ in shape or amplitude while the period of the discharge current remains the same as that of applied voltage. The transition from SP1 to AP1

[a]Author to whom correspondence should be addressed. E-mail: epningwj@scut.edu.cn

discharge is regarded as the first step of the bifurcation. Investigation on discharge asymmetry makes considerable contribution to the initiation mechanisms of nonlinear phenomena, mode controlling methods in DBDs, and relevant industrial applications, from which its significance is guaranteed in the field of applied plasma.

Although it seems, at first glimpse, surprising about the existence of asymmetric discharges in the symmetrically-arranged DBD structures, massive results and explanations proposed in many previous reports have recorded and convinced this unique and fascinating phenomenon.[14,16–19,22–27] By now, the most commonly-accepted explanation for the cause of asymmetric discharge is the effect of residual positive column (generated during the last discharge epoch) at the beginning of a new breakdown process.[14,23,25] To be specific, the residual positive column increases the non-uniformity of spatial electric field distribution prior to the next discharge, preventing the fully development of the discharge process.[22] The residual plasma could also act as an equivalent anode that shortens the effective discharge gap, forcing the discharge to operate in an equivalent Townsend mode, thus initiating a premature current pulse.[25] Those discoveries indicate that, despite the symmetric arrangement of discharge structure, the distribution of such charged particles as electrons, positive ions and the Laplace electric field are actually not strictly symmetric between 2 successive discharge half cycle due to the disturbance of residual positive column,[16,22,23,25,28] and the mismatch of those factors thereupon induce the asymmetry in the parameters of the discharge such as temporal current waveforms and gap voltage waveforms.

However, recent discoveries regarding the effect of residual electrons' motion on DBD dynamics have provided some new possibilities on the inducing factor of discharge asymmetry. Massines *et al.*[29] observed the residual current peaks caused by the electron backflow (i.e. the drift of residual electrons toward the previous cathode boundary due to the inversion of electric field in the gas gap. This phenomenon occurs between the discharge peak moment and the moment of next applied voltage polarity inversion) in DBDs. This implied that the motion of trapped electrons in the discharge space was capable of changing the shape of current pulse. Lee *et al.*[30] and Jiang *et al.*[31] also noticed the residual current peak with one-dimensional fluid models, and their observations further suggested that the backflow of residual electrons could have a significant influence on the upcoming breakdown process. Zhang *et al.*[16] concluded that high seed electron density would reduce the breakdown voltage of subsequent discharge, forming a weak discharge pulse, and then the discharge symmetry was disrupted. Their results provided an important clue to interlink the effect of electron backflow with the discharge asymmetry, since the electron backflow is able to alter the seed electron level of the subsequent discharge, thus probably affecting the discharge asymmetry. Those reports inspire us that, other than the influence of positive column, there might be a new mechanism related to the effect of electron backflow that functions on the discharge asymmetry.

It's worth noting that in our previous report,[15] a preliminary study on the electron backflow indicated that it would always completely dissipated before the next breakdown in a short gap (d=2.08 mm) He DBD, and we concluded the electron backflow had a minor effect on the SP1 to AP1 transition under this specific case. On the other side, we revealed the dissipation rate of the residual electron was slower in larger gap-width (6 mm~10 mm) DBD,[22] which tended to enhance the influence of the residual plasma. Therefore, in this paper, we use the gap width (4 mm~9 mm) as the study variable, by tracing the evolution process of discharge modes between SP1 and AP1 discharges in atmospheric helium DBDs with a one-dimensional fluid model, to study the effect of electron backflow on the discharge asymmetry.

The paper is organized as follows: a brief description of the model and simulation setup are shown in Section II, results obtained in the simulation can be found in Section III. In Section IV, detailed discussions regarding dynamics and subtle mechanisms of the discharge evolution are presented to explain the relevant phenomena shown in Section III. For a clearer expression, we divide Section IV into 3 subsections. Subsection IV A and IV B concentrate on the dynamics and mechanisms related to the evolution from SP1 to AP1 discharge and from AP1 to SP1 discharge, respectively. Connections between electron backflow region and residual positive column with respect to discharge asymmetry are proposed in Subsection IV C. Finally, some conclusive remarks are put forward in Section V.

II. MODEL DESCRIPTION

The atmospheric DBD considered here is generated in pure helium gap between two dielectrically insulated parallel-plate electrodes. The thickness of each dielectric layer (d_b) is 1 mm and the relative permittivity (ε_r) is set to be 7.5, corresponding to the value of mica glass. The width of discharge gap is flexible, with atmospheric helium gas filling in at the temperature of 300 K. Electrodes are considered as disk-shaped, with the area of 0.01 m^2 each. A sinusoidal applied voltage (V_a) with the amplitude (V_{am}) of 2 kV and the frequency (f) of 20 kHz is applied on the left electrode, while the other electrode is grounded. No other external circuit element is introduced to the discharge system. Note that the discharge gap considered in this paper is not very large (under 10 mm), much shorter than the radius of electrodes (about 56.4 mm), therefore, the discharge considered here can be assumed homogeneous radially. Under the conditions mentioned above, a one-dimensional fluid model is appropriate to simulate the discharge process, which has also been successfully applied to predict the nonlinear phenomena in previous reports.[7,15–17,22,25,32,33] The schematic of the model is illustrated in Figure 1.

In this model, electron number density and energy density are determined by the Boltzmann equation, and simplified to the continuity equations through drift-diffusion approximation:[27,34–36]

$$\frac{\partial n_e}{\partial t} + \nabla \cdot \boldsymbol{\Gamma}_e = S_e \tag{1}$$

$$\frac{\partial n_\varepsilon}{\partial t} + \nabla \cdot \boldsymbol{\Gamma}_\varepsilon = S_\varepsilon - \boldsymbol{E} \cdot \boldsymbol{\Gamma}_\varepsilon \tag{2}$$

$$\boldsymbol{\Gamma}_e = -\mu_e n_e \boldsymbol{E} - D_e \nabla \cdot n_e \tag{3}$$

$$\boldsymbol{\Gamma}_\varepsilon = -\frac{5}{3}\mu_e n_\varepsilon \boldsymbol{E} - \frac{5}{3} D_e \nabla \cdot n_\varepsilon \tag{4}$$

where n_e, n_ε represent the electron number density and energy density, respectively. $\boldsymbol{\Gamma}_e$, and $\boldsymbol{\Gamma}_\varepsilon$ are the electron flux vector and electron energy flux vector. S_e is the source term describing the net changing rate of electron density due to chemical reactions, S_ε is the electron energy source term accounting for the loss or gain of energy from elastic and inelastic collisions between electrons and heavy species. μ_e, D_e represent electron mobility and diffusion coefficient, respectively, their values are calculated by Bolsig+[37] and tabulated as the functions of mean electron energy, while these of the heavy particles are taken from literatures.[38,39] $\boldsymbol{E}$ is the local electric field. The term $\boldsymbol{E}\cdot\boldsymbol{\Gamma}_\varepsilon$ accounts for the contribution of Joule heat. With n_ϵ determined, the electron temperature T_e (in K) can be obtained through:[36]

$$\overline{\varepsilon} = \frac{n_\varepsilon}{n_0} = \frac{3}{2} k_B T_e \tag{5}$$

where k_B represents the Boltzmann constant, $\overline{\varepsilon}$ stands for electron mean energy.

For Q heavy species in the mixture, the transport properties of Q-1 species are described by multi-component equation:[27,36]

$$\rho \frac{\partial (w_k)}{\partial t} = \nabla \cdot \boldsymbol{J}_k + S_k \quad k \in (1, 2, ..., Q-1) \tag{6}$$

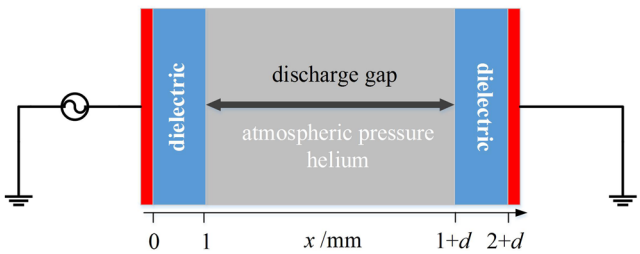

FIG. 1. Schematic of the model. d represents the gas gap width.

where w_k represents the mass fraction of heavy species k, ρ is the density of the mixture, S_k is the source term, $\boldsymbol{J}_k$ represents the diffusive flux vector for species k.[40] The density of the background gas is given by the following equation:

$$w = 1 - \sum_{k=1}^{Q-1} w_k \tag{7}$$

Electric field is determined from Poisson's Equation, describing as

$$\nabla \cdot (\varepsilon_0 \varepsilon_r \boldsymbol{E}) = -\nabla \cdot (\varepsilon_0 \varepsilon_r \nabla V) = \rho \tag{8}$$

where ε_0, ε_r stand for the permittivity of vacuum and relative permittivity, respectively. V is the potential and ρ is the space charge density in the discharge gap.

On the boundaries of the gas gap (i.e. interface with dielectric surfaces), excited species are quenched to helium atom, and secondary electrons are induced by ion bombardment with a emission coefficient γ_i of 0.01, the initial mean energy $\overline{\varepsilon_0}$ is fixed at 2.5 eV. The resulting equations for the normal component of electron flux on the boundaries are given by[27,34,41]

$$\mathbf{n} \cdot \boldsymbol{\Gamma}_\mathbf{e} = \frac{1}{2}\sqrt{\frac{8k_B T_e}{\pi m_e}} n_e - \alpha_s n_e \mu_e \boldsymbol{E} \cdot \mathbf{n} - \sum \gamma_i N_A (\mathbf{n} \cdot \boldsymbol{\Gamma}_i) \tag{9}$$

$$\mathbf{n} \cdot \boldsymbol{\Gamma}_\varepsilon = \frac{5}{6}\sqrt{\frac{8k_B T_e}{\pi m_e}} n_\varepsilon - \alpha_s n_\varepsilon \mu_e \boldsymbol{E} \cdot \mathbf{n} - \sum \gamma_i \overline{\varepsilon_0} N_A (\mathbf{n} \cdot \boldsymbol{\Gamma}_i) \tag{10}$$

where m_e represents electron mass, $\boldsymbol{\Gamma}_\mathbf{i}$ stands for ion flux on the interface, $\mathbf{n}$ is the unit normal vector pointing toward the solid surface, N_A represents the Avogadro constant, α_s is a switching function depending on the product of $\boldsymbol{E}\cdot\mathbf{n}$ defined as

$$\alpha_s = \begin{cases} 1 \ (\mathrm{sgn}(q)\boldsymbol{E} \cdot \mathbf{n} \geq 0) \\ 0 \ (\mathrm{sgn}(q)\boldsymbol{E} \cdot \mathbf{n} < 0) \end{cases} \tag{11}$$

where sgn(q) represents the sign of the charge q for considered species. For heavy species flux, their boundary conditions on the solid surface are described by:[27]

$$\mathbf{n} \cdot \boldsymbol{\Gamma}_k = M_k R_{s,k} + \alpha_s M_k c_k \mu_{k,m} z_k \boldsymbol{E} \cdot \mathbf{n} \tag{12}$$

Where $\boldsymbol{\Gamma}_k$ stands for flux term for species k, M_k, c_k, z_k represent the molar weight, the mass fraction and the charge number of species k, respectively. $\mu_{k,m}$ is the mixture-averaged mobility. $R_{s,k}$ is the relevant surface reaction rate given by[27,42]

$$R_{s,k} = c_k \sum_{i=1}^{N} v_{i,k} \frac{\gamma_m}{1 - \gamma_m/2} \frac{1}{4}\sqrt{\frac{8RT_g}{\pi m_m}} \tag{13}$$

in which N represents the number of surface reactions, R is the universal gas constant, $v_{i,k}$ is the stoichiometric number of species k on the ith surface reaction, γ_m is known as sticking coefficient showing the occurring probability of the reaction, and the term γ_m/(1-γ_m/2) represents Motz–Wise correction.[42] In this paper, γ_m is set to be 1 for all the surface reactions. m_m is the mean mass of the mixture. T_g is the gas temperature, having the assumption $T_g = T_i = T_m = 300$ K. (T_i, T_m are ion temperature and mixture temperature, respectively).

The boundary conditions for surface charge accumulation are given by

$$\frac{d\sigma_s}{dt} = \boldsymbol{J}_e \cdot \mathbf{n} + \boldsymbol{J}_i \cdot \mathbf{n} \tag{14}$$

$$\sigma_s = (\boldsymbol{D}_2 - \boldsymbol{D}_1) \cdot \mathbf{n} \tag{15}$$

where σ_s represents surface charge density, J_e and J_i are the total electron and ion current densities at the wall. D_1 and D_2 are the electric displacement vectors on both side of the boundary. The equations mentioned above are discretized through finite element method. A direct solver PARDISO[48,49] is employed to solve the equation system.

About plasma chemistry, 6 particles, namely the electron (e), He atom, He metastable (He*), He_2 metastable (He_2^*), He^+ and He_2^+, and 15 reactions are considered. Detailed reaction formulas

TABLE I. Chemical reactions considered in the model. T_e denotes the electron temperature in eV. He^* represents $He(2^3S)$ and $He(2^1S)$. He_2^* represents $He_2(a^3\Sigma_u^+)$. n_e is the electron density in m^{-3}. The unit of reaction rate coefficient for two body reactions and three body reactions are m^3/s and m^6/s, respectively. $f(\overline{\varepsilon_0})$ indicates the rate coefficient as a function of the electron mean energy calculated by Bolsig+,[37] and the cross-section data from IST-Lisbon database[47] was used as the input parameter of the calculation.

Num.	Reaction	Rate Coefficient	Energy/eV	Ref.
1	e+He → e+He	$f(\overline{\varepsilon_0})$	/	37
2	e+He → e+He^*	$f(\overline{\varepsilon_0})$	19.82	37
3	e+He^* → 2e+He^+	$f(\overline{\varepsilon_0})$	4.78	37
4	e+He → 2e+He^+	$f(\overline{\varepsilon_0})$	25.6	37
5	e+He+He^+ → He+He^*	1×10^{-39}	0	43
6	e+He_2^* → 2e+He_2^+	$9.75\times10^{-16}\times T_e^{0.71}\times\exp(-3.4/T_e)$	3.4	44
7	e+He_2^+ → He^*+He	$5.386\times10^{-13}\times T_e^{-0.5}$	0	45
8	2e+He_2^+ →He_2^*+e	7.1×10^{-32}	0	43
9	e+He+He_2^+ → He_2^*+He	5×10^{-39}	0	43
10	e+He^* → e+He	4.2×10^{-15}	-19.82	43
11	e+He^+ → He	$1.327\times10^{-27}\times n_e\times T_e^{-4.4}$	-25.6	46
12	e+He_2^+ →He_2^*	5×10^{-22}	-3.4	43
13	He^*+He^* → e+He+He^+	2.9×10^{-15}	/	43
14	He^*+2He → He_2^*+He	1.9×10^{-46}	/	43
15	He^++2He → He_2^++He	6.3×10^{-44}	/	43

are listed in Table I, in which some of the rate coefficient data are calculated by Bolsig+[37] using the cross-section data[47] while others are taken from literature.[43–46] Besides, the initial densities of electron, He^+ and He_2^+ are set to be 2×10^{13} m^{-3}, 1×10^{13} $m^{-}3$ and 1×10^{13} $m^{-}3$ respectively to maintain the initial charge balance. Those initial conditions are common assumptions used in DBD modelling. Within logical parameter ranges, these input values did not show any obvious effect on the solution, just causing minor differences in calculation time.

The equations mentioned above are discretized through finite element method and solved in COMSOL MULTIPHYSICS.[50] A direct solver PARDISO[48,49] is employed in the program to solve the resulting system. For meshing strategy, two extremely fine meshed layers are set in the vicinity of each boundary in order to prevent the oscillation of ion densities in the simulation, each with the length of 0.02 mm and the total element number of 60. The size of mesh in these two layers follows an arithmetic sequence distribution with an element ratio (i.e. the ratio between the size of the largest and the smallest mesh) of 10. The closer the mesh is to the boundary, the smaller its size will be. In the rest of the gap the mesh density is set smaller, with the total mesh number of (d-0.04)*100 and the element ratio of 10. The number of elements in each calculation ranges from 772 to 1020, varying with the gap width, and the number of degrees of freedom varies within 4981~6729. The simulation results obtained under above-mentioned mesh setting have been compared with those yielded from finer mesh calculations, and a maximum difference of 1.5% in current density amplitude was perceived.

The simulation program is executed in a Dell T1700 station (CPU: E3-1226 3.30 GHz, RAM size: 20 G). Over 50 discharge cycles are calculated in each case to ensure that the discharge has evolved into steady state. The time consumption for one calculation (60 cycles) ranges from 30 min to 153 min, depending on the value of external parameters. Typically, a higher d_g leads to a longer calculation time.

To evaluate the accuracy and applicability of this model, we compared the results yielded from our model with those obtained in previous experiments conducted under identical conditions. It is revealed that the simulation results qualitatively agree well with previous pertinent experimental data. Figure 2 shows an example of this comparison, in which Figure 2(a), (b) are previous experimental results reproduced from Ref. 21, whose discharge configuration and external parameters are similar to those of our simulation, and Figure 2(c), (d) are corresponding simulation results obtained from our model. Obviously, the simulation waveforms are qualitatively in accordance with the relevant experimental ones, such as the order of current density amplitudes, the current peak phases, and the ratio between positive and negative current peaks, etc. However, we notice two main discrepancy

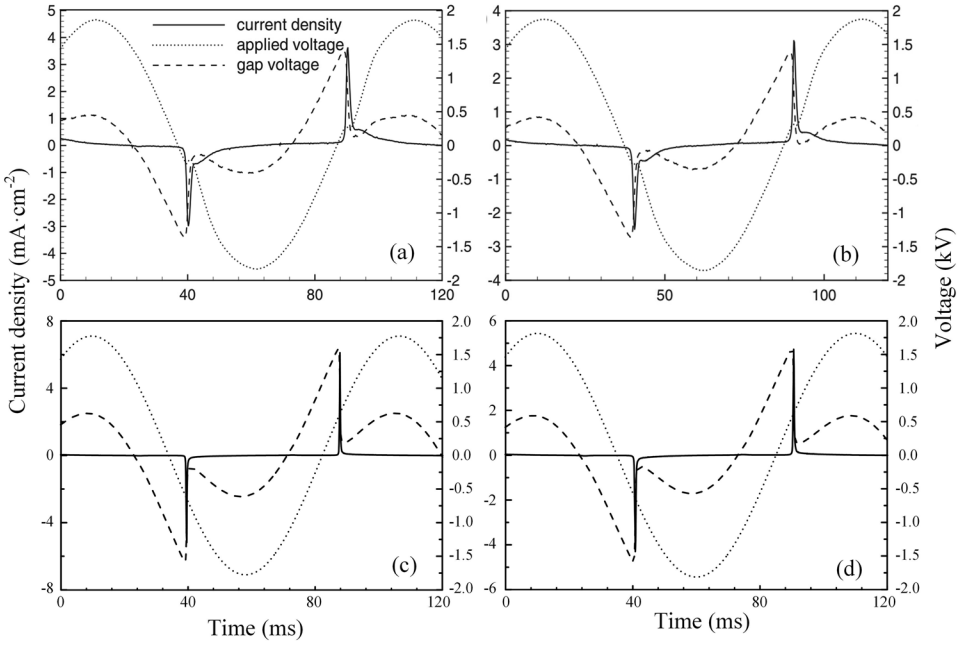

FIG. 2. Comparison between (a), (b) previous experimental waveforms (Reproduced with permission from Mangolini *et al.*, Journal of Physics D: Applied Physics **37**, 1021 (2004). Copyright 2004 IOP Publishing) and (c), (d) their corresponding simulation results obtained from the model described above obtained under identical conditions. The main external parameters in (a) and (c) are: V_{am}= 1776 V, f=10 kHz, d=5 mm, d_b=1 mm; in (b) and (d) are: V_{am}= 1813 V, f=10 kHz, d=5 mm, d_b=1.5 mm.

between our simulation results and Mangolini's. First, the pulse width and absolute current peak value. We figure this discrepancy is attributed to the effect of nitrogen impurities on the ionization and quenching processes and the limitation of energy consumption during the pulsing epoch.[51,52] Second, the current density during the afterglow period, which is mainly attributed to the Penning ionization.[27,52,53]

On top of that, our modelling results also show a good agreement with other pertinent experimental data exhibited in Ref. 14, 54. Note that our main propose in this work is to investigate the basic mechanisms regarding mode transition between SP1 and AP1 discharges, rather than quantitative reproduce some discharge phenomena in experiments, the results obtained from this model should be acceptable. Similar or even simpler models have already been successfully applied to investigate nonlinear behavior of DBD in our previous publications[15,22,32] and in relevant works recently performed by other groups.[7,16,25,33,55]

III. RESULTS

By purposely altering the width of discharge gap d ranging from 4 mm to about 9 mm under the simulation condition described above, we study numerically the discharge asymmetry in atmospheric helium DBDs. The width of the gas gap will affect the breakdown voltage of DBD, and commonly, the wider the gap width is, the higher the ignition voltage will be. In our study cases, namely 2 kV AC and 4 mm-9 mm gap width, the applied voltage is sufficient to ignite the gap, which can been implied by the discharge phase (the phase of the current peak moment). To be specific, the breakdown occurs before the voltage peak for all study cases, and the discharge phase is 9.36°for 4 mm gap and 15.84° for 9 mm gap, respectively. In this regard, the surface polarization plays a significant role in the breakdown process, especially in the shorter gap case with more intense discharge (means more surface charge accumulation). However, if the applied voltage is sufficiently low, the breakdown of the long gap DBD will rely more on the surface polarization. Besides, it is worth noting that the sampling step size of d is not strictly fixed at a constant value. In particular, in the vicinity of

critical gap widths regarding mode transition, the sampling step size is set smaller (around 0.1 mm or 0.05 mm) since the numerical values vary abruptly there. In other gap widths larger step sizes are set.

The judgement of SP1 and AP1 state in this paper is determined by following 2 criteria:

(1) The period of discharge current maintains the same as that of applied voltage.
(2) The discharge current keeps approximately symmetric between positive and negative half cycle, and the ratio of difference between the amplitude of positive and negative current peak (denoted as *Diff*) is less than 2%. Detailed expression of *Diff* is shown as follows:

$$Diff\,\% = \frac{\left|J_{p+} - J_{p-}\right|}{\min\left[J_{p+}, J_{p-}\right]} \times 100\% \tag{16}$$

in which J_{p+} and J_{p-} represent the amplitude of positive and negative current density, respectively. If both 2 criteria are reached, the discharge will be classified as SP1 discharge; if the discharge only meet the requirement of criterion (1), it will be regarded as AP1 discharge; if none of these 2 criteria are met or only criterion (2) are met, the corresponding discharge could be in the state of multi-periodic, quasi-periodic or chaos *etc.*, which are not included in this paper.

When the discharge gap is relatively short (below 5.65 mm), the SP1 discharge is observed in the first place. As the gap width increases further, the discharge symmetry starts to disrupt, while AP1 discharges show up. Figure 3 demonstrates a clear evolution of discharge mode transition shown in waveforms in this stage. In these waveforms, V_a represents the input voltage, and has a perfect sinusoidal waveform since we have ignored the external circuit such as the ballast resistor and stray capacitance. V_g presents the voltage drop in the gas gap, and is calculated from the spatial integral of electric field (E), which is determined by the Poisson's Equation. j is determined by the sum of conductive current density (j_c) and displacement current density (j_d). j_c equals to the sum of electron current density (j_e) and ion current density (j_i), which are derived from the continuity equations. Besides, j_d is determined by the time differential of electric displacement vector (D). In Figure 3(a), (b), the discharges exhibit a standard SP1 feature, in which the gap widths are fixed at 4 mm and 5.6 mm, respectively. Once the gap width reaches 5.65 mm, the discharge transforms into asymmetric state, with a strong current peak in the positive half of the applied voltage cycle and a relatively

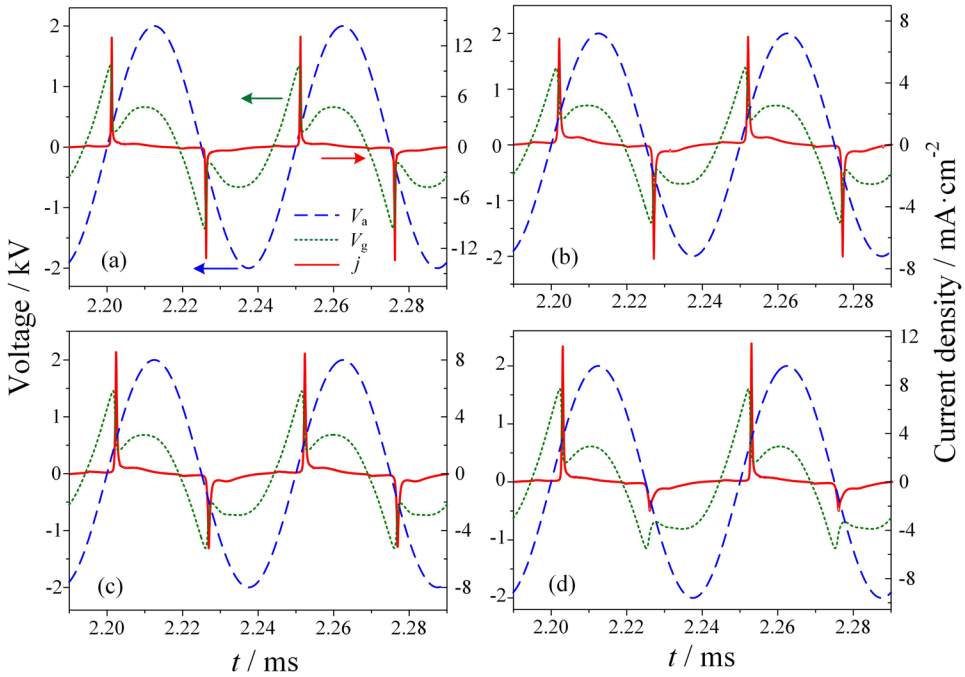

FIG. 3. Temporal profiles of current density (j), applied voltage (V_a) and gap voltage (V_g) when the gap width is fixed at (a) 4 mm, (b) 5.6 mm, (c) 5.65 mm, (d) 6 mm.

weaker one in the negative half cycle, while the period of the current remains the same as that of applied voltage, as illustrated in Figure 3(c). Those are typical characteristics of AP1 discharge in atmospheric DBDs.[14,16,22,25] Further increase the gap width, the discrepancy between the peak value of positive and negative current pulse appears to be more remarkable. Figure 3(d) illustrates the discharge waveform when the gap width is fixed at 6 mm. Compared with Figure 3(c), the positive current pulse is enhanced while the negative pulse is greatly weakened. The transition from SP1 to AP1 state is a typical nonlinear evolution route in DBD system, which has been observed and discussed in numerous previous reports.[14,15,21–25,27]

After evolving into AP1 mode, if continuously enhancing the gap width up to 9 mm, more interesting phenomena can be observed. Figure 4 illustrates the evolution of discharge waveforms when gap width varies from 7.5 mm to 8 mm. Apparently, as the gap width increases, the amplitude of positive current pulse decreases in a large extent (over 60%) in this process, and the difference of amplitude between positive and negative current pulse declines in this process. Finally, a SP1 discharge is yielded when gap width d reaches 8 mm, as shown in Figure 4(d). This unique evolution route is in principle consistent with previous relevant results.[14,21,23]

In order to acquire an overall view of discharge state evolution, complete evolution trajectories of positive and negative current amplitudes (J_{p+} and J_{p-}) varying with gap width are plotted in Figure 5. It is worth noting that the discrete data shown in Figure 5 as well as the following figures are collected under the steady state of the discharge and are averaged in 10 successive applied voltage cycles. As is shown in Figure 5, with the increase of d, the current density of positive and negative peaks decrease synchronously before turning into AP1 mode. While in AP1 mode, the peak value of negative current density decreases dramatically in the vicinity of transition point (5.65 mm), whereas the positive peak curve rises near the transition point and decreases afterwards. In this stage, the difference between J_{p+} and J_{p-} enlarges rapidly around d = 5.65 mm, while saturates and decreases at longer gap widths. As d approaches the critical value of AP1-SP1 transition (8 mm), there exists a dramatic decrease in J_{p+}, while the J_{p-} curve declines slowly at first, then rises slightly in the vicinity of d = 8 mm, as shown in Figure 5(c). In addition, the peak difference is greatly narrowed in this process. Once d exceeds 8 mm, the 2 current density curves converge, as shown in Figure 5(c), and the discharge recovers to SP1 state.

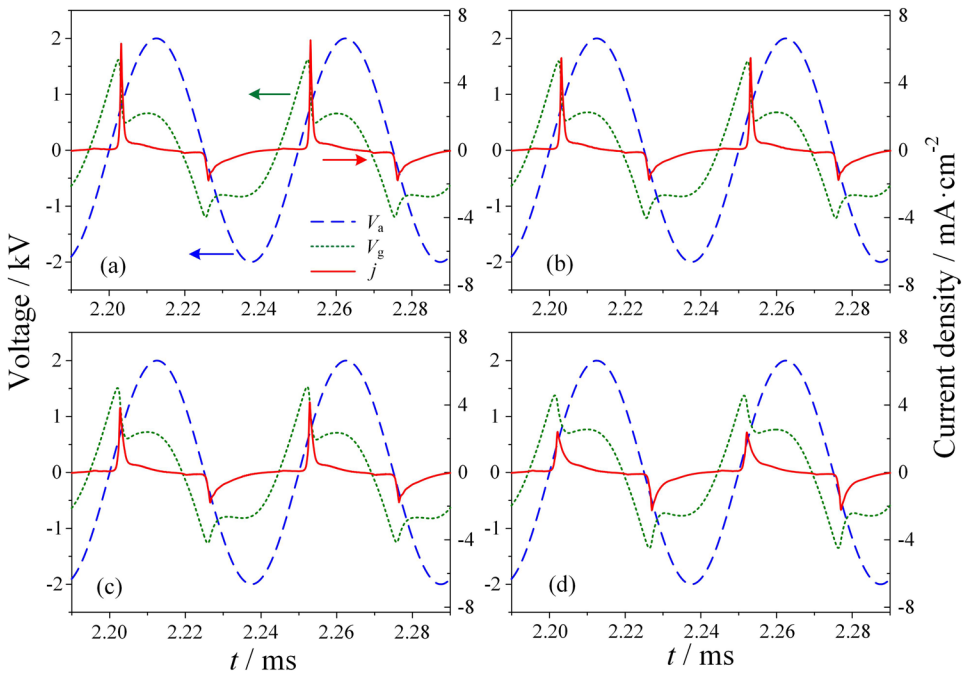

FIG. 4. Temporal profiles of current density (j), applied voltage (V_a) and gap voltage (V_g) when the gap width is fixed at (a) 7.5 mm, (b) 7.7 mm, (c) 7.9 mm, (d) 8 mm.

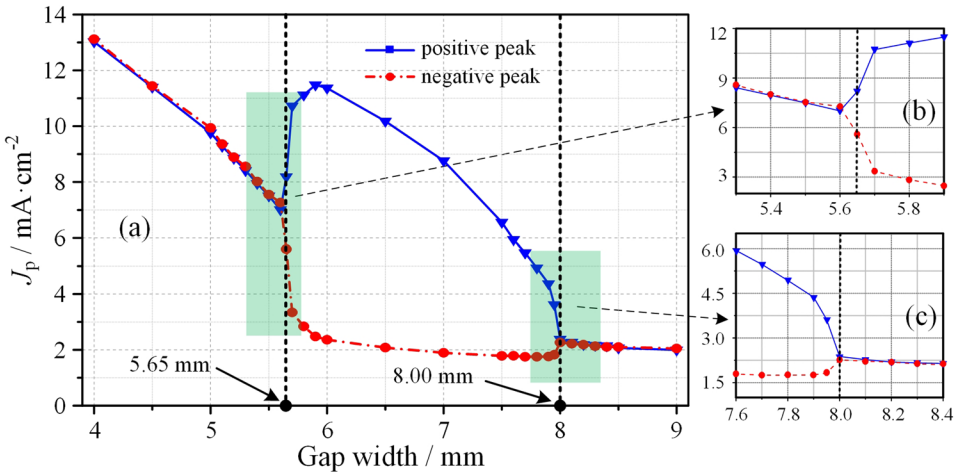

FIG. 5. Evolution trajectories of (a) peak value of current density, as well as (b), (c) their partial zoom-in plots in the vicinity of critical gap widths. The negative peak curves are plotted in absolute value in favor of direct comparison.

IV. DISCUSSIONS

A. Dynamics and mechanisms with regard to SP1-AP1 evolution

In order to uncover the mechanisms concerning SP1-AP1 evolution, we first analyze the spatial structure of discharges in AP1 mode, taking d = 6 mm case as the example. Some key observation moments are set between positive and negative current peak, which are labeled in Figure 6, while their corresponding spatial structures, taking account of electron density (n_e), ion density (n_i) and electric field (E) distributions, are illustrated in Figure 7. Figure 7(a) depicted the spatial structure of the discharge at the positive current peak moment. Obviously, the cathode fall with high electric field and a large ion density, the negative glow where the electric field drops to almost zero, and the positive column where charged particles are in quasi-neutral state while the electric field maintains a relative low constant value, can be clearly observed. Those features indicate that the discharge is operating at glow regime at this moment.[22,23,38,56]

Once the positive discharge pulse is extinguished, the electric field decreases significantly in the cathode fall region due to the charge accumulation on dielectric surfaces, which shields the electric field of the applied voltage. As a result, the spatial structure of previous cathode fall region can hardly sustain, thus the electron density and ion density in this region decline dramatically.[22] Since then, a particle density gradient near the right border of positive column region is gradually formed,

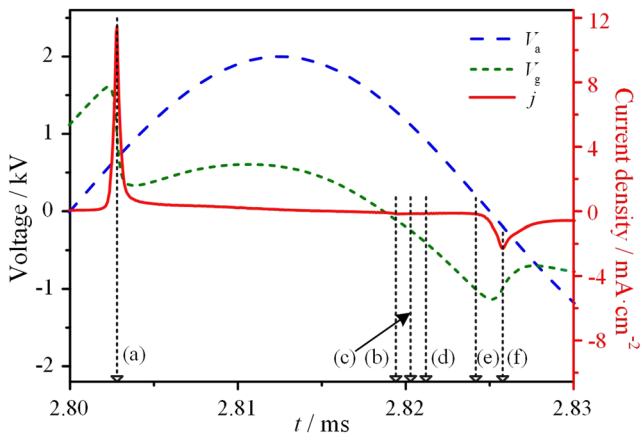

FIG. 6. Arrangement of observation moments (a)-(f) in AP1 discharge.

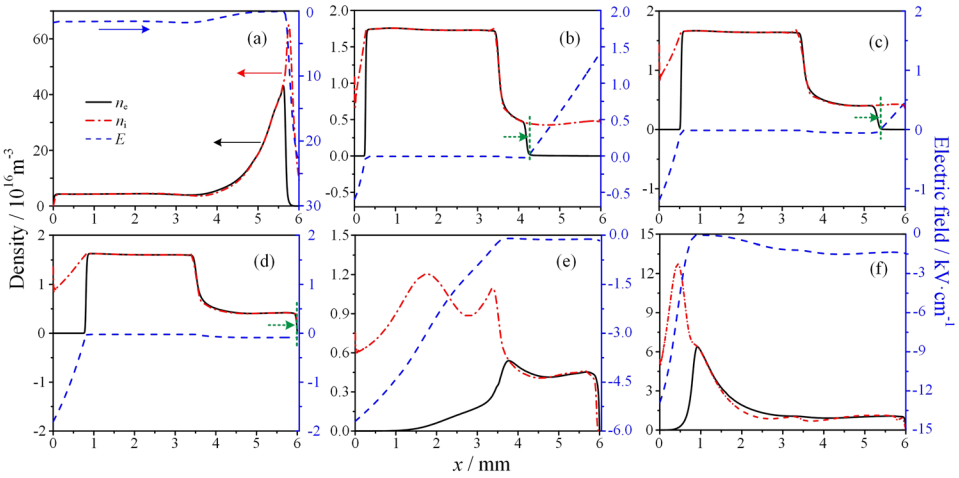

FIG. 7. Spatial distributions of electron density (n_e), ion density (n_i) and electric field (E) in AP1 discharge (d=6 mm) at several key moments (a)-(f) as labeled in Figure 6. The positive direction of E is defined as the direction from x=0 to x=6. The direction of the secondary vertical scale of (a) is reversed in favor of observation and direct comparison with (e). The green arrows and green dashed lines in (b)-(d) illustrate the flowing direction and head position of electron backflow, respectively.

while the neighboring electric field remains a considerably high level. Therefore, the positive column diminishes from the right side because of drift and diffusion of volume charges.[22,23,25,38]

Upon the inversion of gap voltage, the positive column region starts to diminish from the left border. Subsequently, because of inverted electric field among the gas gap and space charge effect, electrons flow back toward the instantaneous anode (x = 6 mm) and shield the residual ions, forming a new plasma region on the right side of the gap, as shown in Figure 7(b), (c), (d). This process is called the electron backflow.[15] Identical phenomena are also observed in previous publications.[15,23,29–31] It is worth noting that the backflow of ions also exists in the relevant phase, however its effect on discharge dynamics is negligible owing to the much lower drift and diffusion rates compared with those of electrons. Therefore, the aspect of ion backflow is not considered here.

Figure 7(e) illustrates the spatial structures of charge densities and electric field strength at the moment when the negative discharge is about to start. As it can be seen, the electron backflow region is not completely diminished, with a residual plasma region in the vicinity of instantaneous anode. Under this circumstance, the development of negative discharge should be effected, since the residual plasma region is capable of restraining the development of electric field among the gap in the breakdown process.[22,25] Figure 7(f) depicted the spatial discharge structure at negative current peak moment. Compared with Figure 7(a), the charge densities and the absolute value of electric field among the cathode fall region in Figure 7(f) decline significantly, but the discharge regime has not changed, still retains its character as a typical glow discharge.

To illustrate the evolution tendency of electron backflow effect in different gaps, the spatial-temporal distribution of electron density in logarithm expression ($\log_{10}(n_e)$) over one discharge period in different gaps are plotted in Figure 8. Inspecting Figure 8, the process of electron backflow can be clearly observed. Moreover, in relatively short gaps (d<5 mm.), the shape of electron areas keep inversely symmetric between positive and negative half cycle, and a narrow electron backflow area is observed. The time interval between the finishing moment of positive electron backflow and the initial moment of negative main discharge is relatively large, as shown in Figure 8(a). As the gap width increases, this interval is shortened, as depicted in Figure 8(b), (c). It is mainly because a wider electron backflow region is formed, thus the dissipation time of electron backflow region is prolonged. When the gap width reaches d = 5.65 mm, as shown in Figure 8(d), the electron backflow area is already connected with the area of negative current pulse, resulting in the disturbance of discharge symmetry. Further increase the gap width, the overlapped area of electron backflow and negative discharge expands, as shown in Figure 8(e), (f), indicating that the width of residual backflow region at the initial moment of negative breakdown expands with increasing gap width. As a result,

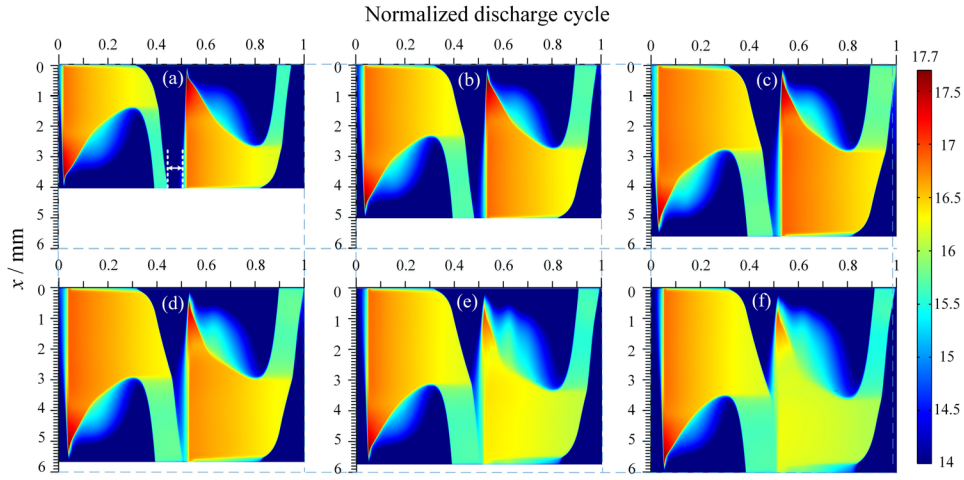

FIG. 8. Spatial-temporal distribution of $\log_{10}(n_e)$ over a discharge period when the gap width d is fixed at (a) 4 mm, (b) 5 mm,(c) 5.6 mm,(d) 5.65 mm, (e) 5.7 mm, (f) 6 mm. The white dashed lines and arrow in (a) illustrate the interval between positive electron backflow area and the area of subsequent negative pulse.

it is predictable that the electron density among the gap when the negative breakdown begins would also be enhanced as d increases. It should be pointed out that the results mentioned above exhibit some distinctive differences with our previous report[15] concerning SP1-AP1 evolution in a short gap (d=2.08 mm) helium DBD, in which electron backflow region generated in one discharge half cycle was always dissipated completely before the next breakdown. Thus, the influence of electron backflow on discharge asymmetry was believed to be minor in that special case. Moreover, the intensity of electron backflow in previous report was impaired when approaching the transition point, while strengthening after evolved into AP1 mode with applied voltage increasing, which is not observed in the present work. Therefore, with different controlling parameters applied in these two works, the electron backflow exhibits some distinctive different behaviors, exerting dissimilar influences on the discharge dynamics.

For more insightful investigations, the spatial distribution of electron density in different gaps at the starting moment of negative breakdown are plotted in Figure 9, from which the tendency of growth in electron density with the increase of gap width is clearly observed. It is worth noting that in this paper, the starting moment of each breakdown is defined as the moment when the minimal value

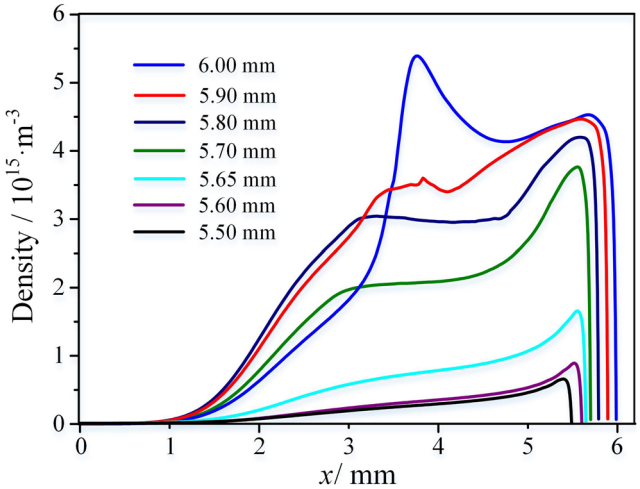

FIG. 9. Spatial distributions of electron density over the gas gap at the starting moments of negative breakdown in different gaps.

of space-averaged electron density is reached between two adjacent main current peak moments. At this moment, the decreasing trend of electron density ceases and the electron begins to proliferate over the gap owning to the intensified ionization process. Moreover, the residual electrons at the initial moment of next breakdown can be considered as the seed electrons of the next discharge.[16,28,57–61] Previous reports have mentioned that high seed electron density restrains the electric field among the gap, reducing the breakdown voltage of subsequent discharge, thus forming a premature discharge pulse,[16,57,62] and such mechanism can be briefly explained as follows. As we know, the electron avalanche plays an important role in the breakdown process. The electron density n_e produced by the avalanche has the form[38]

$$n_e = n_{e0} \exp\left(\int_0^d \alpha \mathrm{d}x\right) \tag{17}$$

where n_{e0} and d are seed electron density and gap width, respectively, α represents the collision ionization rate, having the form

$$\alpha = Ap \exp\left(\frac{-B}{E/p}\right) \tag{18}$$

in which p and E represent the gas pressure and local electric field, respectively. A, B are fit coefficients (constant values). In Townsend theory, the critical condition of self-sustained discharge is given by

$$\exp\left(\int_0^d \alpha \mathrm{d}x\right) = 1 + \frac{1}{\gamma} \tag{19}$$

where γ represents the secondary electron emission rate. When enhancing γ, α can be reduced. In DBDs, however, the circumstance is quite different from that of DC glow discharge. In order to use equation (19) to briefly evaluate the avalanche criteria in this case, γ should be generalized to cover all the processes that provide the secondary electrons to the upcoming discharge, including the residual electrons taken from the electron backflow.[38,57,58,60,61,63] In that case, the enhancement of seed electron level should lead to the increase of γ, allowing the breakdown to be reached in a relatively low value of α among the discharge gap. Now that α is positively associated with E, known from equation (18), the decrease of α among the gap is mainly caused by the decline of local electric field E.[38,57,58] That is, as seed electron increases, the development of electric field among the discharge gap could be restrained in the process of subsequent breakdown.

It is acquired from Figure 7 and Figure 8 that both positive and negative discharge peaks operate in glow mode, in which the electric field is mainly concentrated in cathode fall region with an approximately linear distribution.[38] As a result, the electric field level in each discharges at the moment of current peak can be evaluated by the absolute value of electric field near the cathode, denotes as E_c, which is also the maximum value of E in the gap. Therefore, it is predictable that with the increase of seed electrons, the development of electric field in the process of negative breakdown will be restrained, including that at the moment of negative current peaks. In that case, E_c value will be lowered with the growth of seed electrons.

Figure 10 illustrates the values of E_c at the negative peak moment and the average electron density over the gap (n_{eav}) at the initial moment of negative breakdown in different gaps. The value n_{eav} helps evaluate the seed electron level over the gap. From Figure 10, we can see that n_{eav} rises while E_c decreases with the increase of gap width ranging from 5.5 mm to 6.0 mm. Specifically, upon reaching d=5.65 mm, n_{eav} encounters a dramatically increase in a narrow window as d increases due to the present of extra seed electrons provided by residual electron backflow region. Meanwhile, the E_c curve declines with a large slope. To obtain more insights regarding the influence of dramatic decline in E_c on the discharge current, detailed mathematical expression is required. It is evident that in glow discharges, E_c has an approximate relationship with the current density peak value j_p shown as[38]

$$j_p = (1 + \gamma_i)\mu_+ {E_c}^2 / 4\pi d_c \tag{20}$$

where γ_i, μ_+ represent secondary electron emission rate and drift coefficients of positive particles (i.e. ions), both can be regarded as constant values in a certain discharge system. d_c represents the thickness of cathode fall layer, which in general varies slightly with gap width.[38,64] Although the circumstance of atmospheric pressure glow discharge (APGD) generated by DBD structure is not

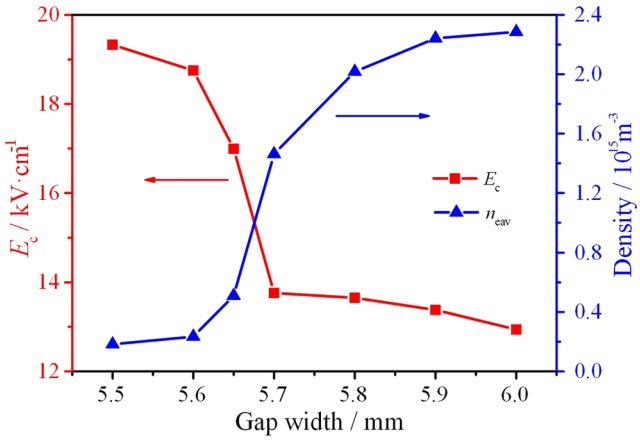

FIG. 10. The average electron density over the gap (n_{eav}) at the starting moment of negative breakdown and the absolute value of electric field near the cathode (E_c) at the negative peak moment in different gaps.

identical with that of DC glow discharge and the utility of equation (20) in a DBD case may not be undoubtedly suitable, our simulation results here, however, just provided a plausible indication about the approximate linear relationship between j_{p-} and E^2 in this APGD case, as shown in Figure 11, in which the simulation values basically in accordance with their j_{p-}~E^2 linear fits. Therefore, we can deduce that when E_c decreases dramatically with the increase of d in the vicinity of d = 5.65 mm, as shown in Figure 10, the decline rate of j_{p-} is almost proportional to that of E^2. This might be the reason why j_{p-} encounters a dramatic descend right after turning into AP1 mode.

As regards positive current pulse, its variation tendency can also be explained by above mechanisms. When increasing the gap width before reaching 5.65 mm, due to the symmetric distribution of particle densities and electric field between positive and negative half cycles, seed electron density for positive current pulse will also be enhanced as that of negative one. Therefore, the peak value of positive and negative current pulses decrease synchronically in this process. Once the gap width exceeds 5.65 mm, the discharge evolves into AP1 mode, in which the symmetric spatial–temporal distribution of particle densities and electric field is disrupted. Note that the negative discharge pulse is weakened, the charged particles generated by negative pulse will also reduce, thus weakening the effect of electron backflow in this discharge phase. In that case, the dissipation time of electron

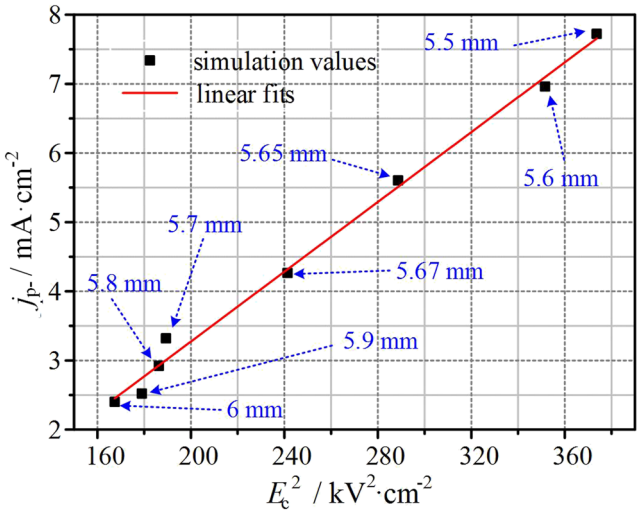

FIG. 11. The relationship between the amplitude of negative current pulse (j_{p-}) and the value of E^2 at the negative peak moment in different gaps, as well as their linear fits.

backflow region will be reduced, prolonging the time interval between the evanishment of electron backflow region and the initial moment of subsequent breakdown. Hence, the residual electron level at the starting moment of positive discharge (i.e. seed electron level) is greatly impaired, which promotes the development of electric field in the process of positive breakdown. As a result, the peak values of positive current pulse is greatly enhanced right after d exceeds 5.65 mm. However, if gap width is increased further, the average electric field $E_{avg} = V_{am}/d$ will decrease to a considerably large extent that offsets the promoting effect of electron backflow, causing the decline of positive current density curve at this stage (d>5.9 mm), as shown in Figure 5(a).

B. Dynamics and mechanisms with regard to AP1-SP1 evolution

It is known from above analysis that the effect of electron backflow has a significant impact on the formation of AP1 discharges. Thus, we may suspect that the electron backflow were also functional in the process of AP1-SP1 transition. To verify this assumption, the spatial-temporal profile of $\log_{10}(n_e)$ in 4 different gap widths, each concludes the time duration of two successive discharge period in favor of observation, are plotted in Figure 12. As expected, significant electron backflow is observed in negative half cycle. Similar to Figure 8, the electron backflow area shown in Figure 12 gradually comes close, finally connects to the area of positive discharge as gap width increases, and their public area expands after the connection. Identical phenomenon is also observed in Ref. 26. Those features indicate that, in a relatively long discharge gap (over 7 mm), a strong electron backflow effect could be induced even in a weak discharge half cycle (i.e. the negative one), and thereby the breakdown process of subsequent discharge may be affected.

Similar to the analysis method applied in section IV A, spatial distribution of electron density over the gap at the initial moment of positive breakdown, as well as the value of n_{eav} and E_c for positive discharge in different gaps, are plotted in Figure 13. Compared with Figure 9 and Figure 10, identical evolution characteristics, namely the boosting of seed electron level and the reduction of electric field E_c with the increase of gap width *etc.*, can be found in Figure 13. Furthermore, it is found the approximate linear relationship between j_p and E^2 proposed by equation (20) is also valid here. As E_c decreases with gap width increasing, applying equation (20), the current density at positive peak moment will also decrease. Therefore, it can be considered that the decrease of J_{p+} discussed here share the same physical mechanism as that of j_{p-} in the process of SP1-AP1 evolution.

It is known from Figure 5(a), (c) that at the stage of AP1-SP1 evolution, as the amplitude of positive current pulse decreases with gap width increasing, the negative current peak experiences a slight growth in the vicinity of d = 8 mm. One possible reason is that, with the decline of positive current

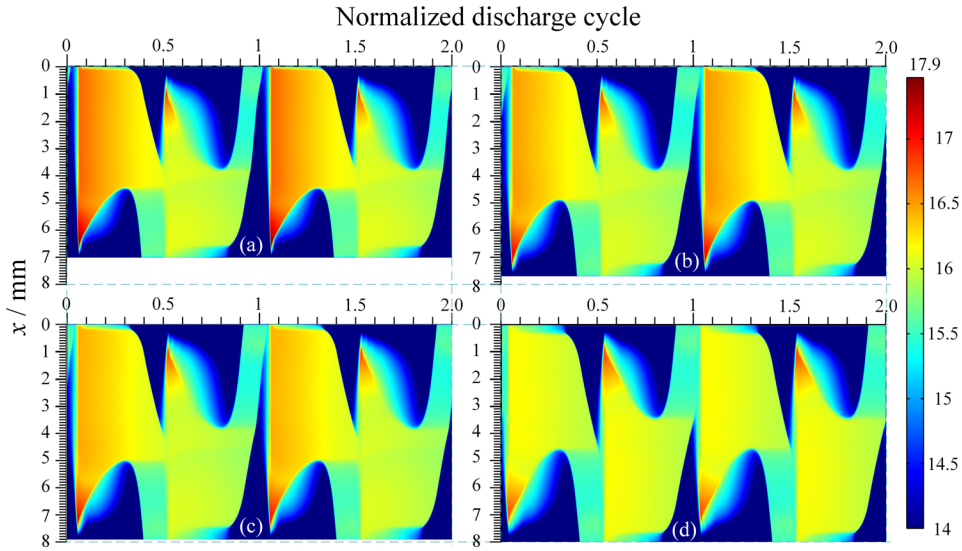

FIG. 12. Spatial-temporal distribution of $\log_{10}(n_e)$ over two successive discharge period when the gap width d is fixed at (a) 7 mm, (b) 7.7 mm, (c) 7.9 mm, (d) 8 mm.

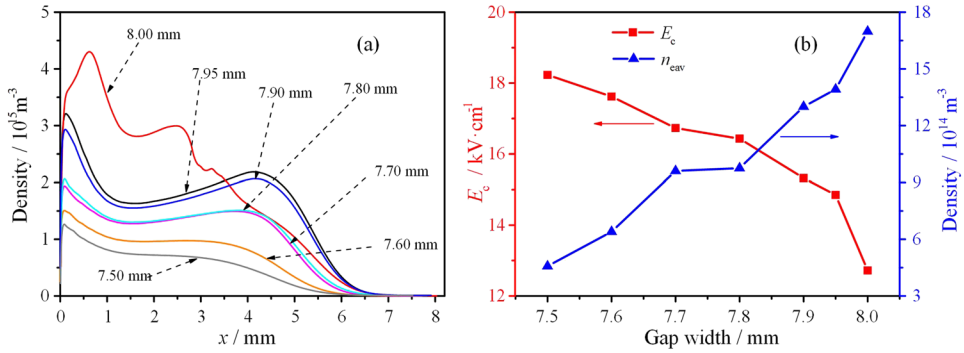

FIG. 13. Spatial distribution of electron density over the gas gap at the starting moments of positive breakdown (a), as well as their average electron density (n_{eav}) and the absolute value of electric field near the cathode (E_c) at the positive peak moment in different gaps (b).

peak, the charged particles generated by positive discharge are also reduced. Thus, the residual electron backflow region at the initial moment of negative breakdown is narrowed, and the seed electron density of negative discharge is suppressed. In that case, the negative discharge is strengthened, hence the difference between positive and negative peaks is reduced. Finally, this discrepancy is basically eliminated as gap width d reaches 8 mm, as shown in Figure 5(c). Symmetric distribution of charged particles and electric field is formed again, and the discharge evolves back to SP1 mode.

C. Connections between the effects of electron backflow and residual positive column on discharge asymmetry

The electron backflow, known from section IV A and IV B, plays an important role in initiating the mode transitions between SP1 and AP1 discharges, while in previous reports, most proposals for the cause of discharge asymmetry rely on the function of residual positive column.[16,22,23,25] Therefore, connections between the functions of electron backflow region and residual positive column on discharge asymmetry are of critical importance for the pursuit of more universal mechanisms. Figure 14 illustrates the spatial-temporal distributions of $\log_{10}(n_e)$ over one discharge period in different gaps under AP1 discharge mode, as well as their relevant spatial discharge structures at the beginning of negative discharge pulses. As is shown in Figure 14(a), (b), (e), (f), in relatively short gaps

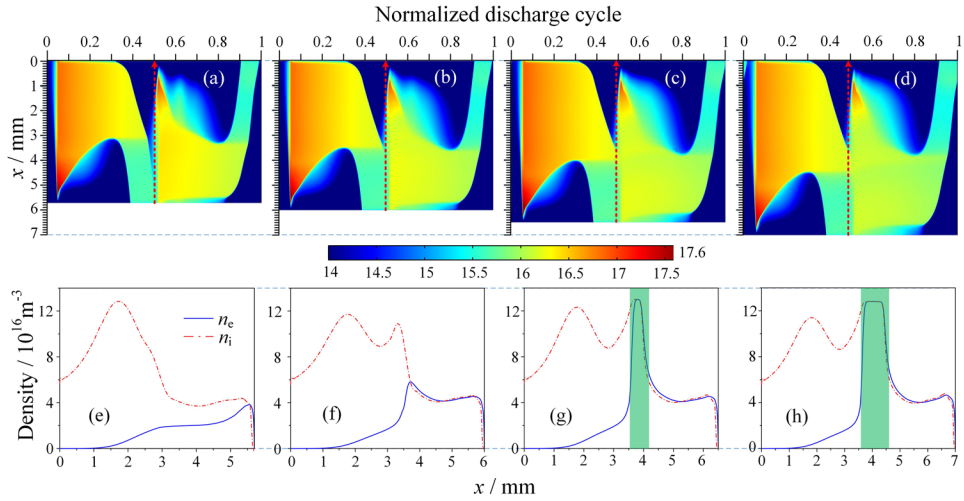

FIG. 14. Spatial-temporal distribution of $\log_{10}$ (n_e) over one discharge period when the gap width d is fixed at (a) 5.7 mm, (b) 6.0 mm, (c) 6.5 mm, (d) 7.0 mm, as well as (e)-(h) their relevant spatial distributions of electron density (n_e) and ion density (n_i) at the beginning moment of negative discharges (labeled in (a)-(d) with red dashed arrows). The greened areas in (g) and (h) highlight the approximate ranges of residual positive column.

(d<6 mm), the residual quasi-neutral regions at the beginning of negative pulses consist of only formal electron backflow region, and we call those the 'backflow-induced' AP1 discharges. As d increases, the residual plasma region expands on its left border, and eventually covers the region where positive column used to locate, as shown in Figure 14(g), (h). Those are typical 'positive-column-induced' AP1 discharges, which are vastly reported in previous studies.[16,22,23,25]

However, it turns out that the residual positive column in a so-called 'positive-column-induced' AP1 discharge should also be regarded as the residual electron backflow region. As shown in Figure 14(c), (d), when the electron backflow is initiated, the trapped electrons all over the gas gap start to move toward the instantaneous anode (i.e. the bottom margin), including those at the position of previous positive column. Meanwhile, the range of plasma region shifts downward. Therefore, the electrons in the so-called 'residual positive column' at the beginning of negative discharge are actually taken from the backflow, rather than directly inheriting local particles from the previous positive column. From this perspective, it could be reasonable that the 'positive-column-induced' AP1 discharge can be classified as a special type of 'backflow-induced' AP1 discharge. This discovery provides a more generalized explanation on the discharge asymmetry and its relevant mode transitions.

V. CONCLUSIVE REMARKS

In this paper, a one-dimensional self-consistent fluid model is applied to investigate the mechanisms of discharge asymmetry and its relevant mode transitions in atmospheric pressure helium DBDs, some important conclusions are listed as follows.

1) By gradually increasing the gap width from 4 mm to about 9 mm, the discharge evolves from SP1 to AP1 mode, and finally returns back to SP1 mode.
2) The SP1-AP1 transition is mainly caused by the existence of residual electron backflow region at the starting moment of negative breakdown. It is the residual backflow region that provides extra seed electrons to the next discharge, restraining the development of electric field in the breakdown process, thus weakening the subsequent negative current pulse. Once the negative discharge pulse is weakened, due to the impairment of charge generation and electron backflow effect, seed electron level for the upcoming positive discharge is also lowered, which further strengthens the positive current pulse. Those mechanisms bring about the inconsistency of positive and negative current pulse, inducing the SP1-AP1 transition.
3) In the process of AP1-SP1 evolution, the residual electron backflow region at the beginning of positive breakdown suppresses the positive discharge process, reinforces the negative discharge, and gradually eliminates the difference between the positive and negative current pulses, thus the SP1 discharge is retrieved in the discharge.
4) By appropriately increasing the gap width in AP1 discharges, a 'backflow-induced' AP1 discharge can be switched to a 'positive-column-induced' AP1 discharge. Moreover, it is revealed that the 'residual positive column' referred in previous publications is essentially a special form of the 'electron backflow region'. As a result, the dynamics of electron backflow provides more universal explanation regarding the mode transitions in DBD with controlling parameters varying.

ACKNOWLEDGMENTS

This work is supported by the National Natural Science Foundation of China (Grant No. 51607074), State Key Laboratory of Alternate Electrical Power System with Renewable Energy Sources (Grant No. LAPS17005) and the Fundamental Research Funds for the Central Universities (Grant No. 2017BQ42).

[1] T. Ito, T. Kanazawa, and S. Hamaguchi, Phys Rev Lett **107**, 065002 (2011).
[2] P. J. Bruggeman, F. Iza, and R. Brandenburg, Plasma Sources Science and Technology **26**, 123002 (2017).
[3] N. Y. Babaeva, C. Zhang, J. Qiu, X. Hou, V. F. Tarasenko, and T. Shao, Plasma Sources Science and Technology **26**, 085008 (2017).
[4] T. Shao, V. F. Tarasenko, W. Yang, D. V. Beloplotov, C. Zhang, M. I. Lomaev, P. Yan, and D. A. Sorokin, Plasma Sources Science and Technology **23**, 054018 (2014).

[5] X. Li, Q. Zhang, P. Jia, J. Chu, P. Zhang, and L. Dong, Physics of Plasmas **24**, 033505 (2017).
[6] J. S. Boisvert, J. Margot, and F. Massines, Plasma Sources Science and Technology **26**, 035004 (2017).
[7] X. Li, R. Liu, P. Jia, K. Wu, C. Ren, and Z. Yin, Physics of Plasmas **25**, 013512 (2018).
[8] S. Pu, J. Chen, G. Wang, X. Li, and Y. Ma, Applied Physics Letters **102**, 194105 (2013).
[9] T. Shao, W. Yang, C. Zhang, Z. Niu, P. Yan, and E. Schamiloglu, Applied Physics Letters **105**, 071607 (2014).
[10] H. Cheng, X. Liu, D. Liu, and X. Lu, High Voltage **1**, 62 (2016).
[11] S. Mohapatro and S. Allamsetty, High Voltage **2**, 69 (2017).
[12] G. Gao, L. Dong, K. Peng, W. Wei, C. Li, and G. Wu, Physics of Plasmas **24**, 013510 (2017).
[13] L. Dong, G. Gao, K. Peng, W. Wei, C. Li, and G. Wu, AIP Advances **7**, 075112 (2017).
[14] D. Dai, Q. Wang, and Y. Hao, Acta Physica Sinica **62**, 135204 (2013).
[15] W. Ning, D. Dai, Y. Zhang, Y. Hao, and L. Li, Physics of Plasmas **24**, 073509 (2017).
[16] D. Zhang, Y. Wang, and D. Wang, Physics of Plasmas **20**, 063504 (2013).
[17] Y. H. Wang, Y. T. Zhang, D. Z. Wang, and M. G. Kong, Applied Physics Letters **90**, 071501 (2007).
[18] H. Shi, Y. Wang, and D. Wang, Physics of Plasmas **15**, 122306 (2008).
[19] Y. Wang, H. Shi, J. Sun, and D. Wang, Physics of Plasmas **16**, 063507 (2009).
[20] J. Zhang, Y. H. Wang, and D. Z. Wang, Physics of Plasmas **20**, 082315 (2013).
[21] L. Mangolini, C. Anderson, J. Heberlein, and U. Kortshagen, Journal of Physics D: Applied Physics **37**, 1021 (2004).
[22] D. Dai, H. X. Hou, and Y. P. Hao, Applied Physics Letters **98**, 131503 (2011).
[23] Y. B. Golubovskii, V. A. Maiorov, J. Behnke, and J. F. Behnke, Journal of Physics D: Applied Physics **36**, 39 (2003).
[24] D. Dai, Y. Zhang, and W. Ning, High Voltage Engineering **43**, 1766 (2017).
[25] Y. Ha, H. Wang, and X. Wang, Physics of Plasmas **19**, 012308 (2012).
[26] J. Zhang, Y. Wang, and D. Wang, Thin Solid Films **519**, 7020 (2011).
[27] C. Lazarou, T. Belmonte, A. S. Chiper, and G. E. Georghiou, Plasma Sources Science and Technology **25**, 055023 (2016).
[28] D. Zhang, Y. Wang, J. Sun, and D. Wang, Physics of Plasmas **19**, 043503 (2012).
[29] F. Massines, A. Rabehi, P. Decomps, R. B. Gadri, P. Ségur, and C. Mayoux, Journal of Applied Physics **83**, 2950 (1998).
[30] D. Lee, J. M. Park, S. H. Hong, and Y. Kim, IEEE Trans on Plasma Science **33**, 949 (2005).
[31] W. M. Jiang, J. Tang, Y. S. Wang, W. Zhao, and Y. X. Duan, Physics of Plasmas **20**, 073509 (2013).
[32] Y. Zhang, W. Ning, and D. Dai, AIP Advances **8**, 035008 (2018).
[33] Z. L. Zhang, Q. Y. Nie, X. N. Zhang, Z. B. Wang, F. R. Kong, B. H. Jiang, and J. W. M. Lim, Physics of Plasmas **25**, 043502 (2018).
[34] W. Yan, Y. Xia, Z. Bi, Y. Song, D. Wang, E. A. Sosnin, V. S. Skakun, and D. Liu, Journal of Physics D: Applied Physics **50**, 345201 (2017).
[35] Z. Huang, Y. Hao, L. Yang, Y. Han, and L. Li, Physics of Plasmas **22**, 1235009 (2015).
[36] M. A. Lieberman and A. J. Lichtenberg, *Principles of Plasma Discharges and Materials Processing*, Vol. 2nd (Wiley, Hoboken, NJ, 2005).
[37] G. J. M. Hagelaar and L. C. Pitchford, Plasma Sources Science and Technology **14**, 722 (2005).
[38] Y. P. Raizer, *Gas discharge physics* Vol. 1 (Springer., Berlin, 1991).
[39] H. W. Ellis, R. Y. Pai, E. W. McDaniel, E. A. Mason, and L. A. Viehland, Atomic Data and Nuclear Data Tables **17**, 177 (1976).
[40] C. Lazarou, D. Koukounis, A. S. Chiper, C. Costin, I. Topala, and G. E. Georghiou, Plasma Sources Science and Technology **24**, 035012 (2015).
[41] G. J. M. Hagelaar, Physical Review E **62**, 1452 (2000).
[42] H. Motz and H. Wise, The Journal of Chemical Physics **32**, 1893 (1960).
[43] M. G. Kong, IEEE Trans on Plasma Science **31**, 7 (2003).
[44] G. Park, H. Lee, G. Kim, and J. K. Lee, Plasma Processes & Polymers **5**, 569 (2008).
[45] X. Yuan and L. L. Raja, IEEE Trans on Plasma Science **31**, 495 (2003).
[46] Y. Wang and D. Wang, Physics of Plasmas **12**, 023503 (2005).
[47] https://www.lxcat.net/ IST-Lisbon database. Accessed on March 27, 2017.
[48] C. G. Petra, O. Schenk, M. Lubin, and K. Gäertner, SIAM Journal on Scientific Computing **36**, C139 (2014).
[49] C. G. Petra, O. Schenk, and M. Anitescu, IEEE Computing in Science & Engineering **16**, 32 (2014).
[50] http://www.comsol.com/plasma-module/.
[51] T. Martens, A. Bogaerts, W. J. M. Brok, and J. V. Dijk, Applied Physics Letters **92**, 041504 (2008).
[52] T. Martens, A. Bogaerts, W. J. M. Brok, and J. van Dijk, Applied Physics Letters **96**, 091501 (2010).
[53] Z. Huang, Y. Hao, Y. Han, L. Yang, L. Tang, Y. Liao, and L. Li, Physics of Plasmas **24**, 113506 (2017).
[54] H. Luo, Z. Liang, B. Lv, X. Wang, Z. Guan, and L. Wang, Applied Physics Letters **91**, 221504 (2007).
[55] S. Gadkari and S. Gu, Physics of Plasmas **24**, 053517 (2017).
[56] Y. H. Wang and D. Z. Wang, Chinese Physics Letter **21**, 2234 (2004).
[57] H. Luo, Z. Liang, X. Wang, Z. Guan, and L. Wang, Journal of Physics D: Applied Physics **43**, 155201 (2010).
[58] H. Luo, X. Wang, and C. Li, Europhysics Letters **97**, 15002 (2012).
[59] T. Shao, R. Wang, C. Zhang, and P. Yan, High Voltage **3**, 14 (2018).
[60] N. Gherardi, G. Gouda, E. Gat, A. Ricard, and F. Massines, Plasma Source Science & Technology **9**, 340 (2000).
[61] N. Gherardi and F. Massines, IEEE Trans on Plasma Science **29**, 536 (2001).
[62] Y. B. Golubovskii, V. A. Maiorov, J. Behnke, and J. F. Behnke, Journal of Physics D: Applied Physics **35**, 751 (2002).
[63] H. Luo, Z. Liang, X. Wang, Z. Guan, and L. Wang, Journal of Physics D: Applied Physics **41**, 205205 (2008).
[64] Y. Hao, B. Zheng, and Y. Liu, Physics of Plasmas **20**, 113510 (2013).